Improving the Aerodynamic Performance of a Cycloidal Rotor through Active Compliant Morphing

Liam Ferrier, Marco Vezza, and Hossein Zare-Behtash

School of Engineering, University of Glasgow, Scotland G12 8QQ, UK

PhD student, l.ferrier.1@research.gla.ac.uk

Abstract

Cycloidal rotors are a novel form of propulsion system which can be adapted to various forms of transport such as air and marine vehicles, with a geometrical design differing significantly from the conventional screw propeller. Research on cycloidal rotor design began in the early 1930s and has developed throughout the years to the point where such devices now operate as propulsion systems for various aerospace applications such as MAVs, UAVs and compound helicopters. The majority of research conducted on the cycloidal rotor's aerodynamic performance have not assessed mitigating the dynamic stall effect which can have a negative impact on the rotor performance when the blades operate in the rotor retreating side. A solution has been proposed to mitigate the dynamic stall effect through employment of active, compliant leading edge morphing. A review of the current state of the art in this area is presented. A two dimensional, implicit unsteady numerical analysis was conducted using the commercial CFD software package STAR CCM+, on a two bladed cycloidal rotor. An overset mesh technique, otherwise known as a chimera mesh, was used to apply complex transient motions to the simulations. Active, compliant leading edge morphing is applied to an oscillating NACA 0015 airfoil to attempt to mitigate the dynamic stall whilst maintaining the positive dynamic Cl contributions. It was verified that by applying a pulsed input leading edge rotational morphing schedule, the leading edge vortex does not fully form and the large flow separation is prevented. Further work in this investigation will focus on coupling the active, leading edge motion to the cycloidal rotor model with the aim to maximise aerodynamic performance.

1 INTRODUCTION

1.1 Cycloidal rotors

Cycloidal rotors are a novel form of propulsion system which can be adapted to various forms of transport such as air and marine vehicles, with a geometrical design differing significantly from the conventional screw propeller. The main advantage of using this rotor system is the instantaneous control of the net thrust vector, meaning that the thrust can be adjusted to any desired direction, perpendicular to the rotor's horizontal axis of rotation. This provides the vehicle with instantaneous 360° control capability to allow for a wide range of possible manoeuvres, for example, achieving Vertical Take-Off and Landing (VTOL) successfully. Controlling the direction of the net thrust vector generated by the rotor can be achieved, either by varying the pitch or phase angle of the

individual blades of the rotor. Examples of different aerospace applications of cycloidal rotors used as primary or secondary propulsion systems are shown in Fig. 1.

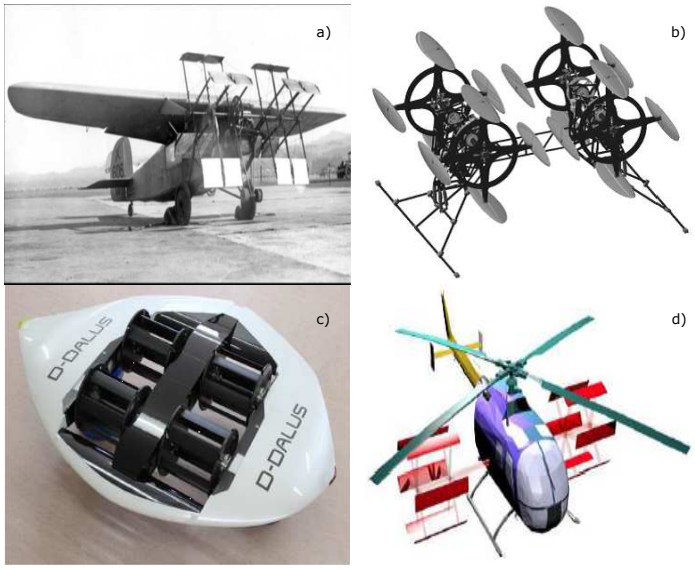

Figure 1: Various aerospace applications for cycloidal rotors: a) The Schroeder cyclogyro [1]. b) Elliptic UAV configuration [2]. c) Small commercial cycloidal rotor application [3]. d) Compound helicopter design [4].

The idea for this novel rotor system originated in the early 1900s and was claimed to be invented by Professor F. K. Kirsten [5] from the University of Washington. The rotor was initially termed as the Kirsten-Boeing Propeller. Throughout the 1930s, further research was conducted at the National Advisory Committee for Aeronautics (NACA) to further develop and understand the aerodynamics and operation of cycloidal rotors. Strandgren [6] developed analytical models to illustrate how the lift and propulsive forces generated by cycloidal rotors were obtained and served as an outline of the general principles and elementary theory of paddle wheels. In his study, he claimed that the vehicle's incidence angle could be changed instantaneously without modifying the orientation of the aircraft, which remained fixed. Wheatley [7] developed a simplified aerodynamic model for assessing the cycloidal rotor performance and for design purposes. In 1934, Wheatley [8] conducted wind tunnel experiments for an 8 ft diameter, 4 bladed, cyclogyro rotor and verified that the cyclogyro would be able to ascend vertically, fly horizontally and glide without power (auto rotation).

In 1998, Bosch Aerospace Inc [9], developed and tested a prototype Curtate, cycloidal propeller to apply to Unmanned Air Vehicles (UAVs). In 2003, Kim [10] conducted a combined CFD and experimental analysis of a cycloidal rotor using a low pitch control mechanism. The blades were manufactured from carbon/epoxy and glass/epoxy composite materials to have sufficient strength against the centrifugal loading acting on the rotor. Extensive numerical and experimental research has been conducted by Hwang on cycloidal rotors for the application of propulsion systems [2] and power generating, high altitude wind turbines [11].

In recent years, interest has grown in a new form of aerospace vehicle called a Micro Air Vehicle (MAV) due to their small scale, low cost for fabrication and the numerous potential applications in both civil and military sectors. MAVs operate in low Reynolds number regimes, where laminar flow mainly dominates the flight regime. Unsteady effects arising from the vehicle's flight mechanics

and environmental issues such as wind gusts have a significant effect on control stability issues of MAVs [12]. Extensive research has been carried out by Benedict et al [13–17] to further understand the aerodynamic and performance characteristics of cycloidal rotors, applied to MAVs.

The wide range of aerospace applications for cycloidal rotors has been further demonstrated by other researchers such as Xisto et al [3, 4, 18] which formed as part of the extensive Cycloidal Rotor Optimised for Propulsion (CROP) project, led by Pascoa [19]. The CROP report, published in 2015, outlined in significant detail the numerical and experimental research conducted on cycloidal rotor propulsion for a wide range of potential applications. Gagnon [4] contributed to this report by developing a simplified analytical model that can be resolved analytically to assess the cycloidal rotors performance as an anti-torque device for a compound helicopter. A visualisation of the proposed helicopter design concept is shown in Fig. 1d.

The majority of the research conducted on the cycloidal rotor's aerodynamic performance have not assessed mitigating the dynamic stall effect which can have a negative impact on the rotor performance. In traditional rotorcraft operation, retreating blade stall is a major limiting factor that constrains the high speed and payload characteristics of the aircraft. During forward flight, the advancing blade experiences an increased velocity due to the positive combination of the rotor rotational velocity and the free-stream air velocity. The retreating blade however encounters a decreased velocity. In order to maintain vehicle stability, the lift generated by the blade has to be equal on both the advancing and retreating side. This results in decreasing the blades incidence angle at the advancing side and increasing the incidence angle at the retreating side. At a specific forward flight velocity, the retreating blade will stall due to the increasing incidence angle and this retreating blade stall effect occurs in all forms of rotorcraft configuration as well as cycloidal rotors. Some of the negative impacts exerted on the aircraft due to the retreating blade stall include buffeting, excessive vibration and large negative pitching moments.

The dynamics of the pitching blade can also generate issues when operating in forward flight. When an airfoil is pitched up rapidly, an over-shoot of the Cl_{max} can occur for an extended incidence angle, also known as dynamic Cl. An overshoot of the Cl_{max} occurs due to a large leading edge vortex forming on the upper surface of the airfoil that separates and travels downstream. As this vortex passes the trailing edge of the airfoil, the flow significantly separates, resulting in a large reduction in lift as well as increasingly negative, nose-down pitching moments. This is known as the dynamic stall effect. It has been observed that employing variable geometry airfoils can be beneficial in optimising the airfoil shape for local flow conditions whilst the blade is under a pitch cycle [20]. Additionally, applying variable, leading edge drooping has illustrated that the severe flow separation could be removed and the dynamic stall effect mitigated for a set range of incidence angle conditions [21].

The main aim of this project is to optimise the aerodynamic performance of a cycloidal rotor using active compliant mechanism structures. This will be achieved by designing and testing efficient, compliant mechanism structures to apply to the leading edge of cycloidal propeller blades for deploying active, variable droop control. The operational procedure is that when the blade transitions into the retreating side, the compliant mechanism will be actuated, resulting in an increasing droop deflection of the airfoil leading edge with the aim of mitigating the dynamic stall effect whilst maintaining the beneficial dynamic Cl characteristics. Once the blade transitions into the advancing side, the drooped leading edge will transform back to its original structure to maintain optimal aerodynamic performance.

1.2 Compliant mechanisms

Compliant mechanisms are single-piece structures which have the primary function of transmitting motion and force mechanically, dependent upon the elastic deformation of their constituent elements [22]. Specifically, they are structures that are geometrically optimised to distribute localised actuation strain to effect a net shape change, deform as a whole and avoid high-stress concentrations on all structural elements associated with the compliant structure [23]. The compliant system consists of smart actuators and sensors embedded within the compliant structure required for motion transmission. Small strains generated by the embedded actuators produce large, global deflections due to stroke amplification from the compliant structure [24]. A visualisation of a simple compliant mechanism used as a gripper is shown in Fig. 2.

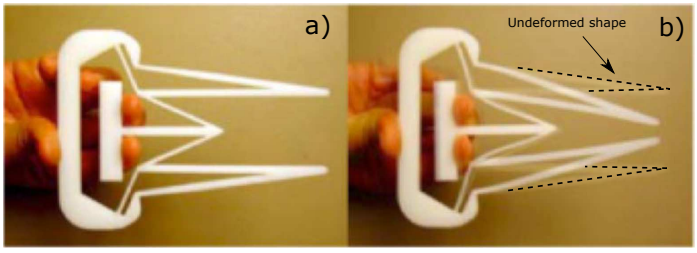

Figure 2: A simple compliant gripper mechanism [23]: a) Gripper position with no actuation force. b) Gripper deflection with actuation force applied.

There are many associated benefits of using flexible, compliant structures to achieve global, continuous shape changes. Firstly, compliant structures are optimised in design to resist deflection under significant external aerodynamic loading and are just as stiff as conventional control mechanisms such as aircraft flaps [23]. Moreover the single-piece design eliminates or reduces the assembly process and various forms of actuator including piezoelectric, shape-memory alloys, and electromagnetic actuators can be embedded within the mechanism. Compliant structures can be fabricated using a wide range of materials including steel, aluminium, nickel-titanium alloys, ABS and polypropylene [23]. The arrangement of material selected for the design within the compliant structure is optimised, resulting in compliance which is distributed so that small strains produce large deformations.

The popular choice of smart actuators that can be embedded within compliant structures include piezoelectric actuators and shape memory alloys. Both forms of actuators are extremely light and compact in size, therefore suitable to couple with flexible structures. Both type of actuators can also be scaled up to a wide range of aerospace vehicles including MAVs, UAVs and transport aircraft as highlighted in an extensive review conducted by Barbarino et al [25].

Shape Memory Alloys (SMAs) are metal alloys that exhibit both the unique characteristics of large recoverable strains and large induced internal forces generated under temperature changes [26]. SMAs possess a unique property termed the shape memory effect [27] which is highly dependent on the alloy temperature. When SMAs reach below a certain temperature, the alloy can be easily deformed and stretched to a new form of configuration which it will retain. When the temperature of the alloy increases by an applied electric current, the alloy will undergo a phase transformation to austenite which results in the actuator returning to its original geometrical configuration. The main advantage of using SMAs as the embedded actuators within compliant mechanisms is the large strain outputs which are generated, however the actuators suffer from very poor frequency responses [27]. Previous experimental research for aerospace application include Manzo [28] who investigated the

feasibility of employing SMA tendon configurations to generate wing morphing rotations in twist and sweep.

Piezoelectric actuators are very popular in electro-mechanical applications due to their high actuation authority and ease of control [29]. The key disadvantages of using piezoelectric actuators are the high power requirements and low actuation strain outputs [29]. There exist various configurations of piezoelectric actuators that have been applied in previously published research in aerospace applications including Active Fiber Composite (AFC) actuators [30], Macro Fiber Composite (MFC) actuators [31, 32] and PostBuckled Precompressed (PBP) actuators [33].

2 NUMERICAL ANALYSIS

2.1 CFD analysis - method procedure

A two dimensional, implicit unsteady numerical analysis is conducted using commerical CFD software package STAR CCM+, on a cycloidal rotor with dimensions taken from Jarugumilli [34]. The model consists of two, NACA 0015 airfoils with a blade span, b = 159 mm, chord length, c = 49.43 mm and rotor radius, R = 76.2 mm. The model dimensions are scaled in this study for application as MAV propulsion systems.

A visualisation of the coordinate system used illustrating the key parameters of a cycloidal rotor system is shown in Fig. 3. The positive lift acts in the positive y-direction and the positive thrust acts in the negative x-direction. Figure 3 also illustrates the blade pitch amplitude, θ, for both blades which will periodically vary over time in a sinusoidal schedule. Ψ represents the rotors azimuthal position and determines the exact position of the blade along the rotor domain. Ψ increases in the clockwise direction, beginning at the frontal, central position of the rotor domain, $\Psi = 0°$. Phase angle, ϕ, is set to 90° that results in both blades achieving peak-to-peak blade pitch amplitudes at azimuthal positions, $\psi = 0°$ and $\psi = 180°$. V_∞ is the uniform free stream velocity with units m/s and Ω is the rotor rotational velocity with units rpm.

In this investigation, prescribed rotational motion and sinusoidal oscillated blade-pitching motion are applied to the cycloidal rotor system to analyse the unsteady, aerodynamic performance characteristics whilst the cycloidal rotor is operating in forward flight. An advanced overset mesh technique is applied in STAR CCM+ to apply transient motion to the simulations. An unstructured, polygonal mesh grid is constructed for both background and overset regions with a prism layer mesher used at the airfoil surfaces. Figure 4a illustrates the generated mesh for the background region and overlap refinement. Large sections of the background domain contain a coarse mesh grid away from the region of interest to allow for any complex flow features produced by the rotor in transient motion to develop over time without large increases in simulation computational time. The overlap section of the background domain containing the rotor has a higher mesh fidelity set to ensure accurate solving of the blade-wake unsteady aerodynamics and flow solver residual stability. The total number of cells generated for both background and overset regions was approximately 137,000 cells and the prism layer characteristics at the airfoil surface was set to ensure wall y+ values ≤ 1 were achieved along the airfoil upper and lower surface.

Figure 4b illustrates the generated mesh grid for the overset region mesh, visualising mesh refinements at the surfaces of both airfoils to ensure an accurate representation of the complex flow features expected to occur. Figure 4b also shows the overset boundary surface which has the primary function of communicating interpolated data between the transient overset region and the background stationary region. The interpolation method for the overset mesh interface was set to linear. Uniform velocity inlet and pressure outlet boundary conditions were applied to the left and

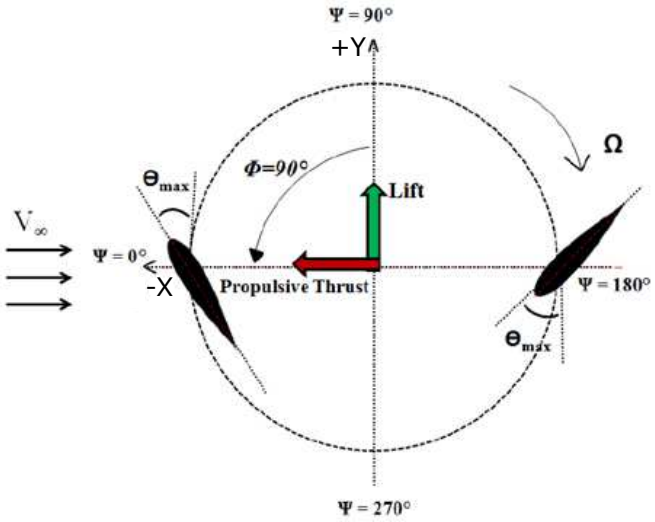

Figure 3: Cycloidal rotor coordinate system for forward flight [34].

right background surface respectively and symmetry boundary conditions were applied to both the background top and bottom surface.

The cycloidal rotor cases investigated in this study were modelled as two-dimensional, unsteady and implicit. Free-stream characteristics were set at sea-level conditions and the density modelled as a constant, incompressible gas. The Spalart-Allmaras turbulence model was employed for URANS closure due to simplicity of implementation, computational efficiency and numerical stability. For the dynamic stall validation cases, the k-ω - SST model was selected due to its more accurate representation of dynamic stall phenomena experienced by oscillating airfoils.

2.2 Validation case - static and dynamic stall

Before assessing the aerodynamic performance characteristics of the cycloidal rotor model, the simulation model was validated against previously published experimental results to assess the flow solution degree of accuracy. The simulation was validated against experimental results obtained from the low speed wind tunnels at the University of Glasgow [35] for a NACA 0015 airfoil under static and sinusoidal oscillated motion conditions. The manufactured model had a chord length, c = 550 mm and span length, b = 1610 mm. For the static case, the Reynolds number and Mach number were Re = 1,514,100 and Ma = 0.1198 respectively at sea-level conditions. The results obtained from the simulation for the static lift coefficient, Cl, and compared against the experimental results is shown in Fig. 5a.

The simulated aerodynamic results in Fig. 5a show good agreement with the experimental results for the majority of incidence angles. The airfoil stalls at approximately 14.5° and the simulated Clmax is underpredicted by approximately 8.1 % in contrast to experimental Clmax. A possible reason for the discrepancy in the Cl results at the incidence angle stall region is due to the flow unsteadiness and the overall coarse mesh grid of the flow domain.

For the dynamic case study, the Reynolds number and Mach number were Re = 1,480,500 and

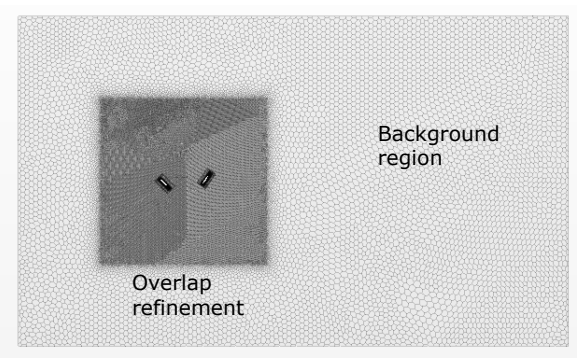

(a) Background region mesh grid view.

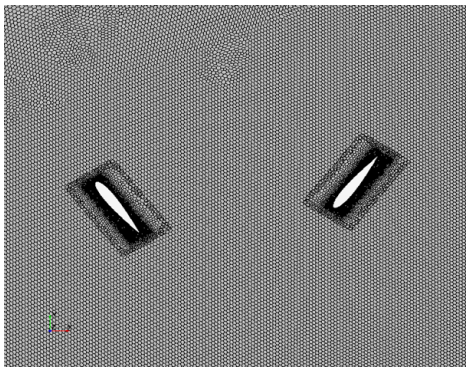

(b) Overset region mesh grid view.

Figure 4: Illustration of the global mesh grid domain and mesh grid containing the airfoil overset regions.

Ma = 0.1174 respectively. The airfoil's transient motion was modelled as a sinusoidal function where the blade's incidence angle, α and angle incidence rate, $\dot{\alpha}$, are defined as follows:

$$\alpha(t) = \alpha_0 \sin((\frac{2\pi}{T})t) + \alpha_M \tag{1}$$

$$\dot{\alpha}(t) = (\alpha_0 \frac{2\pi}{T}) \cos((\frac{2\pi}{T})t) \tag{2}$$

where $\alpha_\circ$ is the incidence angle amplitude in degrees, α_M is the mean incidence angle in degrees, T is the period of the sinusoidal oscillation in seconds and t is time in seconds.

Both $\alpha_\circ$ and α_M are set to 10° which results in the blade exceeding the static stall angle. The pivot point for the airfoil pitching motion is set at 0.25c where the incidence angles are positive in the clockwise direction. The time step is set to T / 4000 and the number of inner iterations set to 5 at each time step to ensure accurate convergence and stability of the flow solution. The number of cycles were set to four to allow for the solution to reach a periodic steady-state however it was observed that the simulation reached a steady periodic convergence after two cycles. The results obtained for the simulated dynamic Cl-α curve against experimental results is shown in Fig. 5b.

Figure 5b shows that the simulated results obtained match well with the experimental results during the upstroke of the sinusoidal oscillation. There is a discrepancy in the Cl results when the airfoil begins the downstroke phase which is the region where the leading edge vortex separates at the trailing edge, resulting in the large rate of loss in lift. The results in Fig. 5b show that lift is increasing beyond the static incidence stall angle and a large positive contribution is generated due to the formation of the leading edge vortex. The small loop which is formed between incidence angles $18° \leq \alpha \leq 20°$ is due to the delay of the leading edge vortex separating from the trailing edge.

2.3 Applying active, compliant leading edge morphing

A simple compliant leading edge morphing motion was applied to the leading edge of the NACA 0015 airfoil which spanned 15 % of the chord length. The maximum leading edge droop was set to 10° identical to ref [21], as dynamically drooped leading-edges have shown to reduce or mitigate

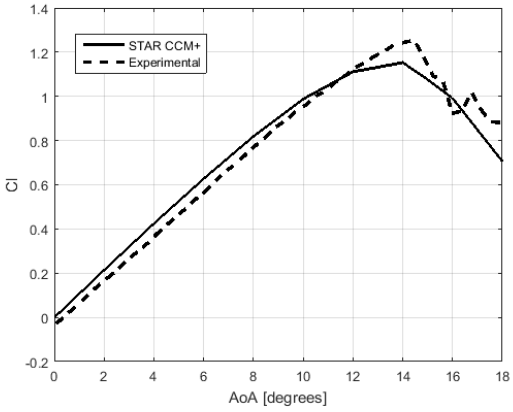

(a) Static Cl comparison.

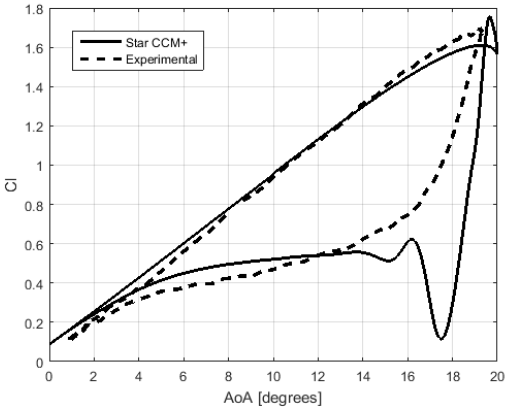

(b) Dynamic Cl comparison.

Figure 5: Static and dynamic aerodynamic characteristics validation: a) Static Cl results. b) Dynamic Cl results.

massive flow separation and the dynamic stall vortex for a given incidence angle. An illustration of the compliant droop pitching schedule as well as the leading edge droop target shape is shown in Fig. 6a.

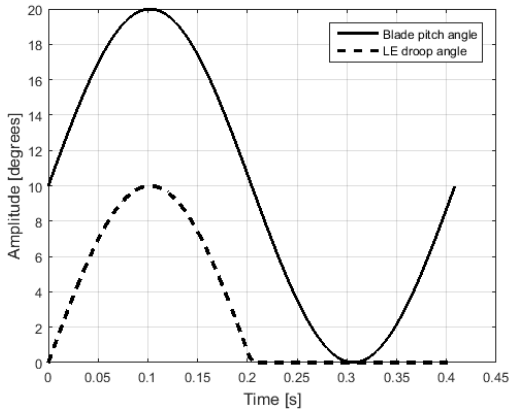

(a) Blade and LE droop pitching schedule.

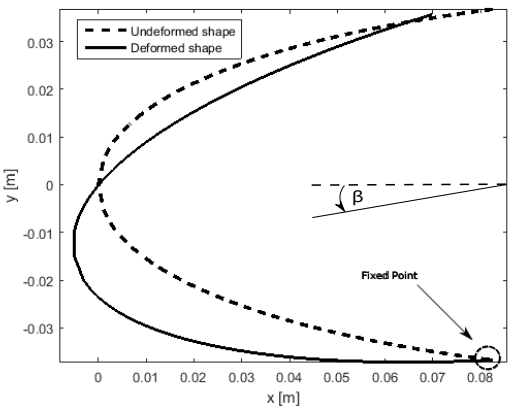

(b) Target shape for 10 degree droop LE.

Figure 6: LE morphing schedule. a) Blade and LE amplitude schedule. b) Target shape for LE morphing.

Figure 6a shows that a pulsed actuation signal is applied to the leading edge droop motion meaning that the morphing motion is only applied during the upstroke phase where the formation of the leading edge vortex occurs. During the downstroke phase when the blade reaches α_M, no morphing is applied. In Fig. 6b, the target deflection required for the leading edge to achieve 10° droop is shown. Figure 6b also shows that positive nose droop, denoted as β, acts in the anti-clockwise direction whereas positive airfoil angle of attack (AoA) acts in the clockwise direction.

The circle marker indicates the fixed position on the body which acts as a hinge point about which all remaining points on the leading edge surface rotationally deform. The morphing increments are imported into the simulation as a function of time and applied as a morphing angular displacement. The morphing method for the intermediate section of the airfoil which incorporates 70 % of the chord is set to floating to adjust its nodal coordinates freely to respond to the leading edge conformal morphing. The morphing method for the trailing edge section which incorporates 15 % of the chord is fixed and follows the sinusoidal motion of the blade along with the overset boundary. This ensures no corruptions of the mesh grid during running of the transient simulations.

The results obtained for the dynamic Cl forces generated by the airfoil for the 4th cycle with active leading edge droop is shown in Fig. 7. It is evident that the large loss of lift due to leading edge vortex dynamic stall is mitigated when active, conformal leading edge droop is applied. This is due to the active morphing at the leading edge suppressing the formation of the leading edge vortex which then travels down to the trailing edge. This is also verified as the morphing results in Fig. 7 show no overshoot dynamic Cl contribution from the leading edge vortex as shown in the case without morphing. A possible reason for the offset in the Cl values at the lower incidence angle range is due to the blade sinusoidal pitching motion causing the flexible leading edge to flex up as no reaction force was applied.

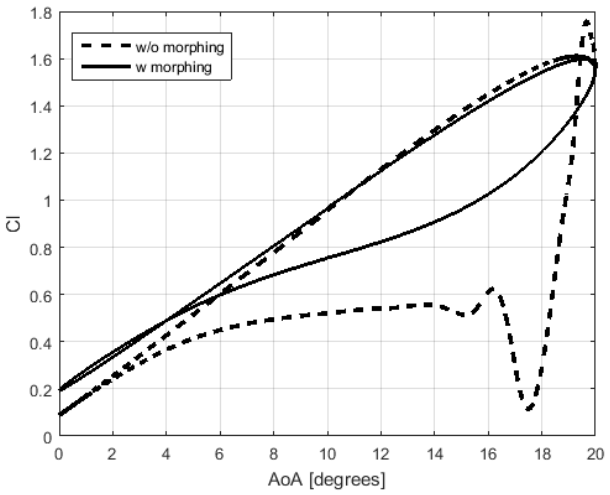

Figure 7: LE morphing Cl comparison. w/o - represents without morphing. w - represents with morphing.

A qualitative assessment was conducted to verify whether applying active conformal leading edge morphing to an oscillating airfoil mitigates or removes dynamic stall. An illustration of the vorticity for both morphing and no morphing cases for a range of incidence angles is shown in Fig. 8. The left column in Fig. 8 demonstrates that when the blade oscillates in the stall region, a leading edge vortex forms which travels to the trailing edge and separates at the beginning of the downstroke. The right column in Fig. 8 verifies that the leading edge vortex is mitigated in the stall region and mild separation occurs.

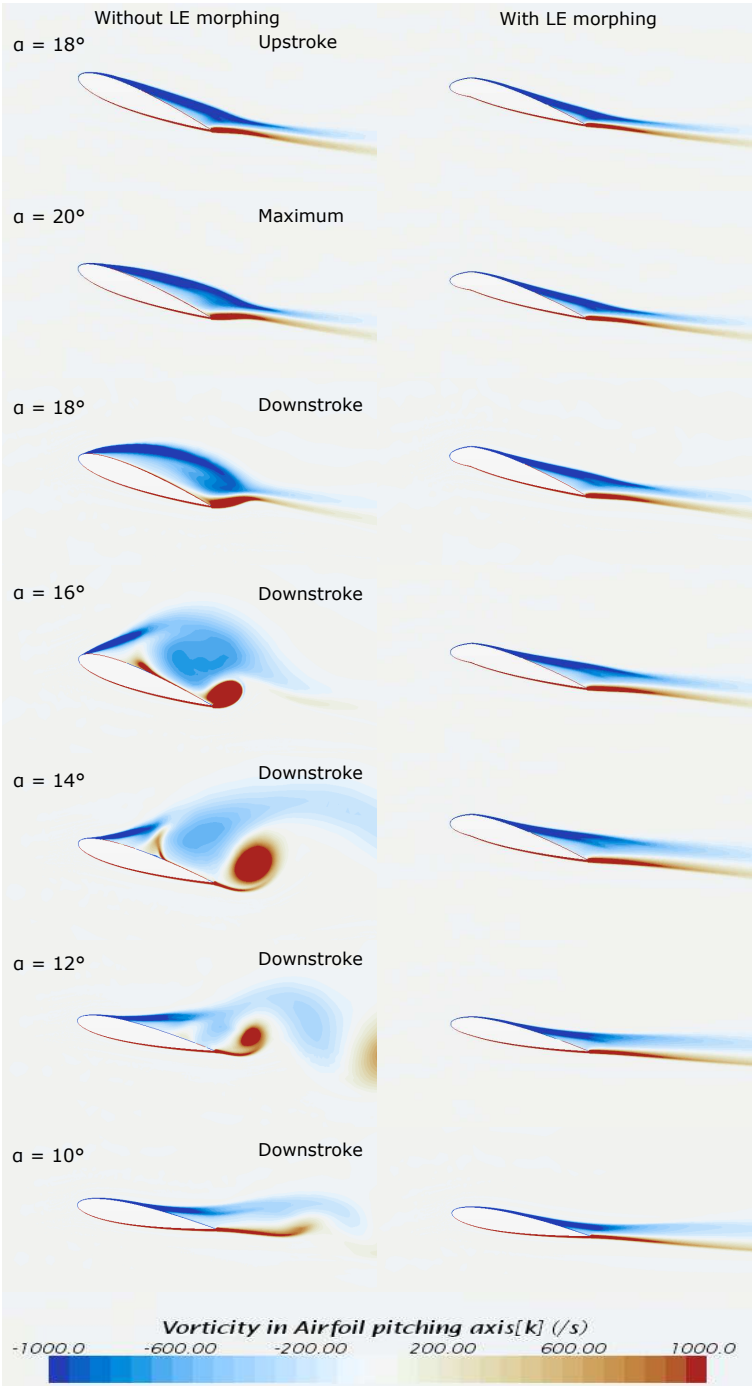

Figure 8: Vorticity comparison with results scaled to illustrate presence of both rotating and counter rotating vortices.

2.4 Cycloidal rotor validation case

For the final case, a parametric study was conducted, varying the rotor advance ratio to assess the aerodynamic characteristics of the cycloidal rotor. The advance ratio, μ, is the ratio of the free-stream airspeed to the rotor tip velocity defined as:

$$\mu = \frac{V_\infty}{\Omega R} \tag{3}$$

where V_∞ is the incoming air velocity in m/s, Ω is the rotor rotational velocity in rpm and R is the rotor radius in m.

Ω and R remain constant at 1200 rpm and 76.2 mm respectively. the only varying parameter is the inlet air velocity which generates three cases of advance ratio that are $\mu = 0.31, 0.52, 0.73$. For the sinusoidal pitching schedule, the maximum blade pitch amplitude was set to $\theta = 35°$ and the phase angle set to $\phi = 90°$. The results for the phase averaged lift generated by the cycloidal rotor blade for the three cases of advance ratio is presented in Fig. 9 as well as the results published by Jarugumilli et al [34].

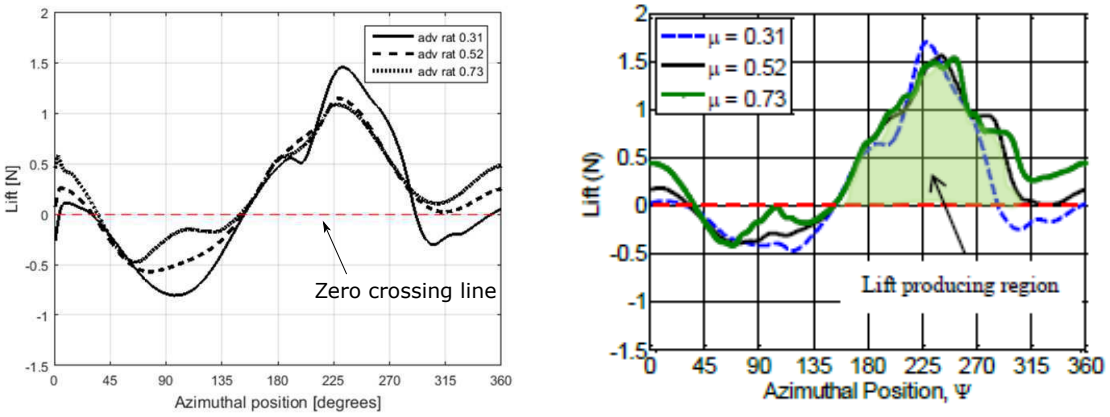

(a) STAR CCM+ results.

(b) validated results [34].

Figure 9: STAR CCM+ results validated against published results by Jarugumilli et al [34] for instantaneous blade lift against rotor azimuthal position for varying advance ratios.

The simulated results in Fig. 9a have validated well against the experimental results shown in Fig. 9b. The rotor retreating side covers the range $0° \leq \psi \leq 180°$ and the rotor advancing side covers the range $180° \leq \psi \leq 360°$. In Fig. 9a, negative lift is generated for all three advance ratio cases at the the rotor retreating side. This is due to the blade's pitch orientation resulting in an decrease in local dynamic pressure resulting in the blade extracting energy from the flow. As the blade transitions into the rotor advancing side, the blade generates a significant increase in positive lift as a factor of the blades pitch orientation, blade-wake interference effects and the local increase in dynamic pressure as the effect of added tangential velocity.

3 CONCLUSION

Cycloidal rotors are a novel form of propulsion system which can be adapted to various forms of transport such as air and marine vehicles, with a geometrical design completely different from the conventional screw propeller. A two dimensional, implicit unsteady analysis was conducted using commercial CFD software package STAR CCM+, on a two bladed cycloidal rotor. An overset mesh technique otherwise known as a chimera mesh, was used to apply complex transient motions to the simulations. The CFD simulation model was validated against experimental NACA 0015 aerodynamic results recorded at the University of Glasgow. Active, continuous leading edge morphing was then applied to the NACA 0015 airfoil, which confirmed that dynamic stall could be mitigated for the case presented. Finally a parametric study involving a variation of the rotor advance ratio on a cycloidal rotor was conducted and validated against experimental results. Future work will incorporate both a review of factors affecting numerical accuracy and morphing topology to establish maximum benefit for aerodynamic performance as well as applying active, compliant leading edge morphing to the cycloidal rotor model.

4 FUTURE WORK

The future steps to be undertaken in this investigation will be to couple the active leading edge morphing motion with the cycloidal rotor model to assess its effect on improving the aerodynamic performance characteristics. Moreover a co-simulation involving software packages ABAQUS and STAR CCM+ will be conducted in the future to perform Fluid Structure Interaction (FSI) simulations of an oscillating blade with active compliant morphing. This two-way coupling process involves a Finite Element Analysis (FEA) to determine key structural parameters such as the blade stress, strain and nodal displacements generated by the external pressure loading, calculated and imported from STAR CCM+. Compliant morphing actuation is applied within the FEA and the morphed structure is exported back into the CFD analysis to re-evaluate the changes in the flow-field characteristics at each time step. The compliant mechanism structural design that will be modelled in ABAQUS will be initially developed using topology optimisation methods [36–38] with the target of finding the optimal actuator positions, minimising actuator effort and maximising the material stiffness to external loading. Analytical models to characterise the force-displacement characteristics of MFC piezoelectric actuators [39–41] will be developed and coupled to the FEA to simulate an accurate representation of compliant mechanisms with embedded, smart actuators. Finally flow visualisation and surface pressure measurement techniques for dynamic stall experiments will be conducted using the low speed wind tunnel test facilities at the University of Glasgow, for a manufactured blade section with a compliant leading edge structure.

5 ACKNOWLEDGEMENTS

The author would like to acknowledge funding via a James Watt Scholarship at the University of Glasgow, grant number - 00227099.

References

[1] Boirum, C. and Post, S. Review of historic and modern cyclogyro design, *45th AIAA/ASME/SAE/ASEE Joint Propulsion Conference & Exhibit*, August 2009, pp 1-11.

[2] Hwang, S., Lee, C.H., Kim, S.J. and Min, S.Y. Development of a four-rotor cyclocopter, *Journal of Aircraft*, November 2008, **45**, (6), pp 2151-2157.

[3] Xisto, C.M., Pascoa, J.C., Abdollahzadeh, M. and Leger, J.A. PECyT - plasma enhanced cycloidal thruster, *Propulsion and Energy Forum*, July 2014, pp 1-13.

[4] Gagnon, L., Morandini, M., Quaranta, G., Muscarello, V. and Masarati, P. Aerodynamic models for cycloidal rotor analysis, *Aircraft Engineering and Aerospace Technology: An International Journal*,2016, **88**, (2), pp 215-231.

[5] Sachse, H. Kirsten-boeing propeller, *TM National Advisory Committee for Aeronautics*, No 351, 1926.

[6] Strandgren, C.B. The theory of the strandgren cyclogiro, *TM National Advisory Committee for Aeronautics*, No 727, 1933.

[7] Wheatley, J.B. Simplified aerodynamic analysis of the cyclogiro rotating-wing system, *TN National Advisory Committee for Aeronautics*, No 467, 1933.

[8] Wheatley, J.B. and Windler, R. Wind-tunnel tests of a cyclogiro rotor, *TN National Advisory Committee for Aeronautics*, No 528, 1935.

[9] Boschma, J. Cycloidal propulsion for UAV VTOL applications, *Technical Report*, 1998.

[10] Kim, S.J., Yun, C.Y., Kim, D., Yoon, Y. and Park, I. Design and performance tests of cycloidal propulsion systems, *AIAA Journal*,2003.

[11] Hwang, I.S., Kang, W. and Kim, S.J. High altitude cycloidal wind turbine system design, *Procedia Engineering*, 2013, **67**, pp 78-84.

[12] McNabb, M.L. Development of a cycloidal propulsion computer model and comparison with experiment, *Mississippi State University*,2001, Master's thesis.

[13] Benedict, M., Ramasamy, M. and Chopra, I. Improving the aerodynamic performance of micro-air-vehicle scale cycloidal rotor: an experimental approach, *Journal of Aircraft*, 2010, **47**, (4), pp 1117-1125.

[14] Benedict, M., Mattaboni, M., Chopra, I. and Masarati, P. Aeroelastic Analysis of a micro-air-vehicle-scale cycloidal rotor in hover, *AIAA Journal*,2011, **49**, (11), pp 2430-2443.

[15] Benedict, M., Jarugumilli, T. and Chopra, I. Effect of rotor geometry and blade kinematics on cycloidal rotor hover performance, *Journal of Aircraft*,2013, **50**, (5), pp 1340-1352.

[16] Benedict, M., Jarugumilli, T., Lakshminarayan, V. and Chopra, I. Effect of flow curvature on forward flight performance of a micro-air-vehicle-scale cycloidal rotor, *AIAA Journal*,2014, **52**, (6), pp 1159-1169.

[17] Benedict, M., Mullins, J., Hrishikeshavan, V. and Chopra, I. Development of a quad cycloidal-rotor unmanned aerial vehicle, *Journal of the American Helicopter Society*,2016, pp 1-12.

[18] Xisto, C.M., Pascoa, J.C., Leger, J.A., Masarati, P., Quaranta, G., Morandini, M., Gagnon, L., Wills, D. and Schwaiger, M. Numerical modelling of geometric effects in the performance of a cycloidal rotor, *11th World Congress on Computational Mechanics*,2014.

[19] Pascoa, J. Cycloidal rotor optimised for propulsion, *Technical report*,2015.

[20] Geissler, W., Sobieczky, H. and Trenker, M. New rotor airfoil design procedure for unsteady flow control, 2000.

[21] Kerho, M. Adaptive airfoil dynamic stall control, *43rd AIAA Aerospace Sciences Meeting*,2005.

[22] Baker, D. and Friswell, M.I. The design of morphing aerofoils using compliant mechanisms, *19th International Conference on Adaptive Structures and Technologies*,2008.

[23] Kota, S., Osborn, R., Ervin, G. and Maric, D. Mission adaptive compliant wing - design, fabrication and flight test, *NATO*,2014, pp 1-19.

[24] Kota, S., Hetrick, J., Li, Z. and Saggere Tailoring unconventional actuators using compliant transmissions: design methods and applications, *IEEE/ASME Transactions on Mechantronics*,1999, **4**, (4), pp 396-408.

[25] Barbarino, S., Bilgen, O., Ajaj, R.M., Friswell, M.I. and Inman, D.J A review of morphing aircraft, *Journal of Intelligent Material Systems and Structures*,2011, **22**, (9), pp 823-877.

[26] Barbarino, S., Ameduri, S. and Pecora, R. Wing chamber control architectures based on SMA: numerical investigations, *International Conference on Smart Materials and Nano Technology in Engineering*,2007, **6423**, pp 1-8.

[27] Seow, A.K. and Liu, Y. Shape memory alloy as actuatore to deflect a wing flap, *49th AIAA/ASME/ASCE/AHS/ASC Structures, Structural Dynamics, and Materials Conference*,2008.

[28] Manzo, J., Garcia, E., Wickenheiser, A. and Horner, G.C. Adaptive structural systems and compliant skin technology of morphing aircraft structures, *Smart Structures and Materials 2004: Smart Structures and Integrated Systems*,2004, **5390**, pp 225-234.

[29] Hagood, N., Kindel, R., Ghandi, K. and Gaudenzi, P. Improving transverse actuation of piezoceramics using interdigitated surface electrodes, *Smart Structures and Intelligent Systems*,1993, **1917**, pp 341-352.

[30] Moses, R.W., Wieseman, C.D., Bent, A.A. and Pizzochero, A.E. Evaluation of New Actuators in a Buffet Loads Environment, *Smart Structures and Materials 2001: Industrial and Commercial Applications of Smart Structures*,2001, **4332**, pp 10-21.

[31] Bilgen, O., Kochersberger, K.B. and Inman, D.J. Novel, bi-directional, variable camber airfoil via macro-fiber composite actuators, 2009.

[32] High, J.W. and Wilkie, W.K., Method of fabricating NASA-standard macro fiber composite piezoelectric actuators, *NASA TM*, 2003, TM-212427, pp 1-30.

[33] Vos, R., Barrett, R., de Breuker, R. and Tiso, P. Post-buckled precompressed elements: a new class of control actuators for morphing wing UAVs, *Smart Materials and Structures*,2007, **16**, (3), pp 919-926.

[34] Jarugumilli, T., Lind, A., Benedict, M., Lakshminarayan, V.K., Jones, A.R. and Chopra, I. Experimental and computational flow field studies of a MAV-scale cycloidal rotor in forward flight, *69th American Helicopter Society International Forum*, 2013.

[35] Green, R.B, Galbraith, R.A.McD., Niven, A.J. The convection speed of the dynamic stall vortex, *Technical Report, University of Glasgow, Department of Aerospace Engineering*,1992.

[36] Kota, S., Hetrick, J., Osborn, R. et al. Design and application of compliant mechanisms for morphing aircraft structures, *Smart structures and Materials: Industrial and Commercial Applications*,2003, **4054**, pp 24-33.

[37] Xinxing, T., Wenjie, G., Chao, S. and Xiaoyong, L. Topology optimisation of compliant adaptive wing leading edge with composite materials, *Chinese Journal of Aeronautics*,2014, **27**, (6), pp 1488-1494.

[38] Sun, R., Chen, G., Zhou, C., Zhou, L. and JinHui Multidisciplinary design optimisation of adaptive wing leading edge, *Science China Technological Sciences*,2013, **56**, (7), pp 1790-1797.

[39] Latalski, J. Modelling of macro fiber composite piezoelectric active elements in abaqus system, *Maintenance and Reliability*,2011, **4**, (4), pp 72-78.

[40] Bowen, C.R., Giddings, P., Salo, A. and Kim, H.A. Modeling and characterization of piezoelectrically actuated bistable composites, *IEEE Transactions on Ultrasonics, Ferroelectrics and Frequency Control*,2007, **58**, (9), pp 1737-1750.

[41] Latalski, J., Georgiades, F. and Warminski, J. Rational placement of a macro fibre composite actuator in composite rotating beams, *Journal of Physics: Conference Series*,2012, **382**, pp 1-6.